Article:
Naderi, S., Dean, J.S. and Zhang, M. (2019) Three-dimensional virtual microstructure generation of porous polycrystalline ceramics. Ceramics International, 45 (17, Part A). pp. 21647-21656. ISSN: 0272-8842

https://doi.org/10.1016/j.ceramint.2019.07.162

Three-Dimensional Virtual Microstructure Generation of Porous Polycrystalline Ceramics

Sadjad Naderi [a, *], Julian S Dean [b], Mingzhong Zhang [a, *]

[a] *Department of Civil, Environmental and Geomatic Engineering, University College London, London WC1E 6BT, UK*

[b] *Department of Materials Science and Engineering, University of Sheffield, Sheffield S1 3JD, UK*

Abstract

Various numerical methods have been recently employed to model microstructure of ceramics with different level of accuracy. The simplicity of the models based on regular morphologies results in a low computational cost, but these methods produce less realistic geometries with lower precision. Additional methods are able to reconstruct irregular structures by simulating the grain-growth kinetics but are restricted due to their high computational cost and complexity. In this paper, an innovative approach is proposed to replicate a three-dimensional (3D) complex microstructure with a low computational cost and the realistic features for porous polycrystalline ceramics.

We present a package, written in MATLAB, that develops upon the basic Voronoi tessellation method for representing realistic microstructures to describe the evolution during the solid-state sintering process. The method is based on a cohesive prism that links the interconnect cells and thus simulates the neck formation. Spline surfaces are employed to represent more realistic features. The method efficiently controls shape and size and is able to reconstruct a wide range of microstructures composed of grains, grain boundaries, interconnected (open) and isolated (closed) pores. The numerical input values can be extracted from 2D imaging of real polished surfaces and through theoretical analysis. The capability of the method to replicate different structural properties is tested using some examples with various configurations.

Keywords

Porosity; Grain growth; Sintering and Shaping.

[*] *Corresponding authors.*
E-mail address: s.naderi@ucl.ac.uk (S. Naderi); mingzhong.zhang@ucl.ac.uk (M. Zhang)

1. Introduction

The significant effect of microstructural heterogeneities on material processing explains why it is essential to generate digital materials which statistically correspond the real microstructures and moreover correlate the digital description to finite element (FE) simulations. Microstructures are generally implemented to FE models by two strategies. First, microstructural properties are implicitly considered in constitutive equations, and second, structural features are explicitly modelled [1-5]. Sometimes, the first strategy is associated with multiple simplifications and causes a high computational cost, especially in non-linear problems. To solve the issue, the second strategy as an alternative method can increase the accuracy and reduce the computational cost using a geometry model with realistic features.

To replicate a microstructure, there are two main approaches including image-based and virtual generation method. In comparison among these two approaches, virtual microstructure generation is much faster and more cost-effective against an image-based method, which typically depends on complex processes such as sample fabrication, image digitalization and model reconstruction. Besides, the desired number of models with comparable structural properties can be produced independently of any pre-existing image. However, a proper algorithm is essential in the procedure of virtual generation to achieve an exact representation of the real microstructure and this paper is concentrated on this matter.

Microstructure modelling approaches can be used for a wide range of applications in different fields such as generation of polycrystalline materials [6-9], porous geometry [10, 11], particulate composites [12-14] and cellular structures [15, 16]. Voronoi tessellation method (VTM) has been broadly considered to model the microstructures of porous polycrystalline materials [17, 18]. Even in an image-based software like DREAM.3D [19], VTM is associated with digital image processing to replicate a fully dense polycrystalline microstructure [20, 21]. DREAM.3D as a commonly known package reconstructs an accurate realistic model, but they are still limited by the image resolution. Briefly, VTM is a discretisation of a domain into a number of cells using a set of seed points; there is one cell for each seed, consisting of all points closer to that seed than any other [22]. Mathematically it can be expressed as:

$$\{R_{P_i}\} = \{x \in \Re^3 : \|\boldsymbol{P_i} - \boldsymbol{x}\| \leq \|\boldsymbol{P_j} - \boldsymbol{x}\|\} \quad (1)$$

$j = 1, 2, \dots, N : j \neq i$

where $\boldsymbol{P_j}$ is the position of the j-th seed points, R_{P_i} is the cell related to the position $\boldsymbol{P_i}$, and $\boldsymbol{x}$ is the position of a generic point in $\Re^3$.

As shown in Figure 1, the generated Voronoi cells can be morphologically similar to a grain, pore or particle [23]. However, in some cases, polygonal or polyhedron shape of Voronoi cells does not appropriately represent a structural attribute and a better description of the geometry with more details is required. For example, in a FE simulation of mechanical behaviour of a porous brittle material, sharp corners and edges of the Voronoi-shaped pore can generate a local stress concentration or even induce a singularity and as such large numerical error in the solutions. In the previous work [10], 2D Voronoi diagram was associated with B-Spline curve [24] to improve the shape and eliminate the sharpness of polygonal pores. Another limitation of this and other similar approaches [25-27] is the weak relationship between the model and the underlying physical background of microstructure formation. It has remained a challenge to form a strong connection between the input for a finite element model and realistic materials processing. The current work aims to develop an approach to simulate porosity inspired by microstructure evolution during ceramics processing.

A microstructure is a signature of the ceramic's processing. Sintering as a part of processing plays a key role in how pores or grains are formed through a microstructure. The main role of sintering is increasing density by decreasing surface energy to the highest possible level [28]. Many applications desire 100% of theoretical density for improved performance [29], but in other applications, porosity can be required such as bio-scaffolds, bone replacements, filters, etc. [30]. Pressureless sintering can be mainly categorized into solid-state and liquid phase process.

Sintering theory has been developed continuously, but the prediction of microstructure evolution has been always challenging even during solid-state sintering of ceramics in a simple case. Different theories were used to treat sintering and they presumed extremely simplified geometries of two or three spherical or composition of other idealized geometries with a number of diffusion paths to analytically predict shrinkage rates [31-33]. Recently, numerical simulation approaches have been broadly developed to model sintering such as FE methods [34], micromechanical approach [35], molecular dynamics simulation [36], continuum thermodynamics

solution [37] and unit cell solutions [38]. The main objective of these works is to provide insights and more exact solutions to this problem. However, their complication and high computational cost limit their use to model the real microstructure evolution mechanism.

The current paper is mainly concerned with solid state sintering. The background will be briefly presented related to pore morphology evolution during sintering in the following section. The purpose of this work is to introduce a new methodology for the accurate geometry model of porous polycrystalline ceramics using VTM inspired by a sintering process. The constructed microstructures can be exported to FE calculations in order to perform various types of material characterisation.

2. Background

There have been several theories to describe pore morphology during sintering process [39, 40]. Solid state sintering and microstructure evolution process are geometrically described in three stages based on the theoretical models as illustrated in Figure 2a. The initial stage is enlargement of the contact areas between particles and creation of necks due to diffusion, vapour transport, plastic flow or viscous flow [41]. For a powder system consisting of spherical particles, neck growth in contact area during densification process is a notable attribute. In the second stage, a tubular interconnected pore network (open porosity) is formed. A different regime is observed in the final stage which tubular pores disappear gradually and then turn to closed (isolated) form at the corners of grains. Based on the theories of pore closure [42, 43], an idealised grain structure in the second and third stages is a tetrakaidekahedron with the pores on edges and corners (Figure 2b). Tetrakaidecahedron or truncated octahedron is a polyhedral geometry with 36 edges, 14 faces including 6 squares and 8 hexagons.

The presence of grain boundaries in polycrystalline materials dictates how the pores are shaped. Therefore, geometry of grains and their interconnectivity are important characteristics in microstructure of a sintered ceramics. Therefore, we focus on modelling grain boundaries and neck formation. The proposed approach is a cost-effective computational framework since it is inspired by physical process but is not coupled with the complex physical theories which would increase the computational cost.

3. The computational approach

In the previous work, the composition of the Voronoi diagram and B-spline curve were used to model 2D irregular porous structure [10]. The generated Voronoi-spline cells (VSC) represented pores and were subtracted from the domain. On the contrary, here, 3D VSCs represent grains and porosity will be available space formed between interconnected grains. The basic approach to generate VSCs was elaborated in [10] but for making the current article self-contained, the principle is presented with the complement explanations for other developments in 3D. Afterwards, a methodology to interconnect VSCs and model neck formation will be described. The previous and current approaches have been coded and developed in MATLAB. All models were meshed using the mesh module in MATLAB by tetrahedral elements.

3.1 Generation of Voronoi-spline cell

The main procedures to construct VSCs are described in the following:

I. *Seeding generator points:* a random set of points are produced in a domain. The points form the centroid of Voronoi cells. In the following steps, it will be shown how generator points induce different structural behaviour to a model and control grain shape, distribution and size.

II. *Discretisation:* the spatial domain is tessellated into Voronoi cells and a series of compartments are created. Figure 3 shows that various discretization systems are implemented into the models using different sets of generator points. An individual module is added to the code in order to seed the points based on an arbitrary distribution pattern. The generator points are scattered according to either a semi-regular (Figure 3a) or an irregular pattern (Figure 3b). The type of pattern influences on the general shape of Voronoi cells in the whole domain. For instance, as seen in Figure 3b, a set of points, which are *randomly* distributed, generate cells with an *irregular* polygonal shape. Also, weighted distribution helps to locally control the cell size. For example, seeding a greater number of points in a region results in the smaller Voronoi cells in comparison to other regions in a domain (Figure 3c). Thus, seeding the generator points plays a leading role in the modelling process and utilization of this technique enables to imitate a variety of microstructures.

III. *Loop subdivision surfaces:* the method is generally used to generate smooth surfaces from arbitrary initial meshes. This technique allows representing surfaces of any complexity with a single B-spline surface using few control points [44]. Each subdivision step results in a new control mesh and a smoother surface. The rules to compute new control points are based on Loop's algorithm [45] which include two main steps. The first step is subdividing a triangulated control mesh of Voronoi cells using quadrisecting each face and connecting edge midpoints as shown in Figure 4a. The second step is computation of vertex positions as a weighted average of old adjacent positions. The weights allocated to the old vertices are named *masks*. To compute the new geometry, two sets of vertices are updated; the edge midpoints generated from the previous step and the original vertices. Figure 4b shows the two types of masks used in Loop's algorithm. The vertex mask applied to an original mesh vertex, are calculated as follows:

$$\alpha = \left(\frac{3}{8} + \frac{1}{4}\cos\frac{2\pi}{n}\right)^2 + \frac{3}{8}$$
$$\beta = \frac{1}{n}(1-\alpha) \tag{2}$$

where n denotes the number of neighbours.

Therefore, new sets of edge midpoints V_A^* and the original vertices V_{ORIG}^* are computed from the old original vertices, V^O, as:

$$V_A^* = \frac{3}{8}(V_B^O + V_C^O) + \frac{1}{8}(V_D^O + V_E^O)$$
$$V_{ORIG}^* = \alpha V_{ORIG}^O + \beta \sum_{i=1}^{n}\left(V_{NBR,i}^O\right) \tag{3}$$

As seen in Figure 5, the subdivision technique defines a smooth surface as the limit of a sequence of successive refinements. The increasing number of subdivision levels results in a well-behaved mesh but at the same time, the number of elements increases. Therefore, iteration number of subdivision should be reasonably selected to avoid expensive computations. In this paper, two iterations are considered.

No intersection occurs between adjacent cells as the splined surfaces are constructed inside Voronoi cells (Figure 6). This method is not either implicit or parametric but due to code and

numerical simplicity, it can be an effective tool for controlling the shape parameters such as roundness and sphericity.

IV. *Scaling:* the control points and the centroid are used to scale a unit cell. First, the cell centre position u_c is calculated from Equation (4) and second the scaled cell vertices obtained from Equation (5).

$$u_c = \frac{1}{m}\sum_{i=1}^{m} u_i \tag{4}$$

$$u_i^{new} = u_c + q(u_i - u_c) \tag{5}$$

where u_i and u_i^{new} are the coordinates of the original and scaled vertices respectively. m is number of vertices in each cell and q is the scale factor which varies between 0 to 1, as the original cells are only allowed to be shrunk to prevent intersection.

Figure 7a exemplifies how a unit cell is schematically scaled and Figure 7b shows how the cells in the entire domain are scaled down with respect to their original size.

3.2 Geometric analogy

To simulate the necking formation, a geometric analogy is introduced between Coble's geometrical model [43] and Voronoi cells. As shown in Figure 2b, grain geometries can be represented by the truncated polyhedrons. There is a geometric analogy between polyhedral shape of Voronoi cell and tetrakaidecahedron. In Figure 8, to highlight the similarities, the truncated polygons are simply subdivided into two segmentations. From this point of view, the structure can be potentially defined by either regular or irregular polyhedral Voronoi cells which are interconnected by prismatic geometries. A prism is simply defined as a solid object with identical ends, flat faces, and the same cross section all along its length. The methodologies to reconstruct VSCs and the code abilities for controlling the shape and size are the basis of the model and will be developed based on the geometric analogy.

3.3 Cohesive prism insertion

To connect two adjacent Voronoi cells by a prism, the interfaces are firstly detected by finding the shared vertices (Figure 9a). Then, a new set of vertices are duplicated with the same coordinates but different indices for each cell (Figure 9b). The cell connectivity is updated by the new vertices. Afterwards, new connectivity is defined between the new vertices to generate the cohesive

interface prism (CIP). It results in two cells being connected via a CIP. CIP is characterised by L_e which is the distance between the centroids of two end shared faces. L_e equals to zero meaning that the cells are directly connected with no prism. L_e automatically changes when Voronoi cells size changes. For instance, by shrinking the cells, CIPs are consequently elongated and L_e increases (Figure 10).

The last stage is fitting B-Spline surfaces through the Voronoi cells and the CIPs. In advance, the cells and CIPs are merged by removing the end faces of prisms. This step is essential to generate a continuous splined surface at the boundaries of cells and CIPs. Figure 11 shows the examples of the adjacent cells and the CIP merged with and without the end faces, and it indicates how this matter influences on the produced geometries.

A pore network is automatically reconstructed by applying the subdivision surface technique to the merged Voronoi cells and CIPs. A sample of the structure generated by 100 cells and $q = 0.95$ is illustrated in Figure 12.

4. Model configurations

4.1. Cell size distribution

Figure 13 simply shows the typical densification curve of a powder compact through three overlapping stages versus sintering time [28]. During the second stage, when interconnected pores are formed, the relative density increases up to ~93%. The final stage includes densification from the open/closed pore state to final densification. Due to this high density and the low volume fraction of necks, the equivalent grain size distribution calculated from the experimental measurements can be potentially used as an initial configuration for the original Voronoi cells. Thus, the VTM is the first key to correlate real and virtual microstructure. In some cases, a VTM underestimates the variability in size and overestimates the number of faces of the grains [46]. However, between randomly produced morphologies, the VTM has the advantage of replicating a wide range of variability of both the size and shape of the grain [47]. In general, VTMs have been successfully verified with experimental data in several case studies some of which have been mentioned earlier.

Either grain size distribution or average equivalent grain size can correspond to Voronoi cell distribution or mean cell size. As an example, one of the simple methods to obtain the average

equivalent grain size, $\bar{G}$, is the broadly accepted Mendelson linear intercept technique [48]. It contains counting the number of grain boundaries intercepted (N) by straight lines of total length L on SEM images with a magnification M and can be expressed as:

$$\bar{G} = 1.56\left(\frac{L}{MN}\right) \quad (6)$$

where the correction factor, 1.56, is imposed due to the three-dimensionality of the grains [27]. Moreover, the grain size can be reported as an Equivalent Spherical Diameter (ESD). This is the diameter of a sphere having the same volume of the grain. It can be measured by some methods like 2D or 3D image analysis [49, 50].

The Voronoi cell size and shape can be implicitly controlled by imposing constraints on the nuclei seeding procedure. To understand the effect of seeding points mode on controlling the cell volume distribution around the mean value, an approach is proposed by introducing a degree of irregularity in the structure. It allows the generator points to migrate from the initial positions according to a semi-regular distribution. The degree of displacement of the seed points is controlled by three random variables, a distance d that is distributed normally and angles θ and φ which are uniformly distributed between 0 and 2π. The effect of irregularity on the tessellated models is shown in Figure 14. The probability density function (PDF) curve against the normalised cell volume indicates that by increasing the irregularity in the microstructure, the number of cells with the average size decreases. For a very irregular mode, grain size distribution can be a better way for experimental verification.

4.2 Neck size

During pore closure, the pore channels are disconnected and become isolated while necks grow. Coble modelled the shape changes using two simple geometries through the second and the third stage sintering based on body centred cubic (bcc)-packed tetradecahedron grains with cylinder-shaped pores along all of the grain edges (Figure 2a). According to Coble's model and the analogy mentioned above, it is possible to adjust channel size by regulating a CIP. D and $2r$ can be interpreted as the size of end faces of a CIP and L_e, respectively. r is related to the scale factor (q) and the mean cell size ($\bar{G}$), as shown in Figure 15 and expressed by:

$$r = \frac{\bar{G}}{2}(1 - q) \tag{7}$$

Depending on a case, the value of r can be theoretically calculated from a neck growth law under different sintering mechanisms such as vapor transport, grain boundary, volume and surface diffusion [41]. The end faces size of the CIP depends on L_e and it cannot be adjusted directly. As an example, by decreasing L_e, the end faces are simultaneously extended (Figure 10), which leads to shrinking of the channels. It should be noted that the tubular shape of pores changes to the closed form when r is very small and q nearly equals 1. In reality, the shrinkage of the interconnected pores is not uniform due to the non-constant size of the pore channels and complexity of microstructures. In order to model such a variable behaviour, q can either randomly changes in an arbitrary range for each cell. If for example, q varies between 0.8 and 1, both types of interconnected and closed pores are possibly reconstructed.

In Figure 16a-c, the 3D cross-sections are presented to show three different porosity systems include open, closed and hybrid open-closed pores. For visual and quantitative comparison with the real 3D microstructure, an example is provided in Figure 16d [51]. The perovskite $La_{0.6}Sr_{0.4}Co_{0.2}Fe_{0.8}O_{3-\delta}$ (LSCF) as a porous ceramic was sintered at 1200 °C. The microstructure of volume of interest 20×15×20 μm was reconstructed using focused ion beam/scanning electron microscope (FIB/SEM) tomography technique. The relative density of the specimen is 84.8±1.2% and the grain size reported as ESD is 1700±630 nm. As it is seen, the virtual models can be morphologically compared to the actual irregular microstructure. Another example is presented in Figure 16e [52] to demonstrates the similarity in two dimensions. The image shows the real microstructure consisting of grain, grain boundaries and pores after incomplete elimination of porosity. It is to be reminded that the structures of grain and the neck were merged in the model through the splining process (Figure 11). So, the grain boundaries are not explicitly displayed although they implicitly exist in the virtual microstructure.

4.3 Effect of number of control points

By fitting the spline surfaces through the vertices of the polyhedral cells, the angular shapes are transformed into rounded structures. Simultaneously, however, the surface area of the original cell is reduced, and the cell becomes smaller. The transformation level can be *implicitly* regulated

by number of control points. To generate more points on the faces, the Voronoi cells are re-meshed by smaller elements before splining surfaces. Figure 17 indicates how the additional number of control points preserves the size and shape similar to the original polyhedral cell. This technique modifies the grains shape when it is more like a polyhedron (Figure 17c) than an irregular particle (Figure 17a or b). Also, the overall density can raise as the grain size is relatively increased. However, the additional points made by more elements drastically increase the computational cost.

5. Examples and discussion

In a microstructure composed of irregular shapes in the form of either grains or pores, the definition or simulation of shape is therefore inevitably complex. The main advantage of the proposed modelling approach is controlling the shape and size of an irregular microstructure to replicate closely what is observed experimentally. The efficiency of the approach has been tested on simulating relative density, which is an important property of a porous microstructure. It should be noted that no statistical analysis has been done because we only propose to describe how the model works and is not possible to cover all possible extensive variation of models generated by different configurations.

The cubes with a dimension of 50 units were tessellated with a semi-regular distribution pattern and two irregularity degrees as we defined earlier ($d = 0$ and 0.01). Figure 18 shows how the number and size of the cells change for 11 samples. The Voronoi cells become smaller by increasing the number of cells but for these specific examples, the average cell size does not change by increasing irregularity. For more than 400 Voronoi cells, the mean cell size does not vary significantly, and cell size distributions are mostly uniform. Figure 18b shows the relative density values against the average equivalent cell size for different scale factors q as it was typified in Figure 16: Two constant values of q were used for producing the open (0.8) and closed (0.99) porosity; The variable q between 0.8 and 0.99 leads to the open-closed porosity system. The relative density is the ratio of the grain volumes to the volume of the cube. The grain volumes are computed by the volume of the solid tetrahedral elements. The average equivalent cell size equals to an effective radius of a sphere with a volume as same as Voronoi cell. To avoid

complexity, r is assumed to be a function of the average equivalent cell size and q instead of an independent input.

As observed in Figure 18, the smaller cells make a model denser in comparison to the coarse cells. An upper and lower bound can be defined for the relative density for each configuration. For a given q, the microstructure is allowed to be regulated in the range between minimum and maximum density by changing the mean cell size. It allows the modelling to have greater flexibility in terms of size control. It is noticeable that the densities of the irregular and semi-regular models are mostly identical except close to the lower bound where more scattering is seen. q can be properly used as the initial estimation of the relative density because of its deviation from the mid-ranges and the maximum values. For the open porosity model, q is 2% and 3% less than the mid-range (0.82) and the maximum value of the relative density, respectively. For the open-closed porosity system, the mean value of q (0.9) is 3% and 2% less than the mid-range (0.87) and the maximum value, respectively. In the closed porosity system, the mid-range (0.94) and the maximum values are 5% and 3% less than q, respectively; the relative density varies with a smaller amplitude (0.05 units) in comparison with other systems (0.1 units).

The relative density 84.8±1.2% reported in Figures 16d can be achieved by the configurations used in this example. This density value is equivalent to the density of typical ceramics in the last stage of sintering in reference to the range specified by the densification curve (Figure 13). By increasing the sintering temperature up to 1200 ^{o}C, more pore connectivity was observed in the LSCF specimen [51]. Therefore, according to Figure 18b, the corresponding model can be set up by either $q = 0.8$ and the mean cell size of 8.71 unit, thereby giving the density of 84.31%; or $0.8 < q < 0.99$ with the mean cell size of 20.73 unit and the density of 84.83% (in both settings $d = 0$). The dimensions of the model and the real sample can be compared if 1 unit is assumed to be 1 μm. It is found that the average cell size is greater than the actual size of grains based on the ESD value equal to 1.7±0.63 μm. Although, if required, it is certainly expected that the average equivalent cell size is regulated by decreasing the dimensions of the cube from 50^3 to 20^3 μm^3 and increasing the number of cells more than 450.

If one of the following states is found, the increase of control points helps to regulate the model: q and the mean cell size either must be fixed or cannot change anymore; less rounded

grains are needed. To exemplify, a microstructure as a basic model is constructed by q of 0.8 and 93 Voronoi cells with the mean cell size of 14.7. The density is raised by adding the control points in 10 steps. Figure 19a depicts that 3% density increment is achieved. The numbers of elements are shown as labels on the data points are seen to be growing at the same time as the number of control points, up to ~3.6 times more than the basic model. It consequently increases the time length of the model generation. The times reported in Figure 19a are based on simulation on an ordinary laptop computer (DELL Latitude 7490) configured with Intel® Core™ i7-8650U 1.90 GHz processor and 16.0 GB RAM. It is noteworthy that if the mesh module available in MATLAB or even the mesh technique to generate tetrahedron elements was replaced with more efficient one, the times and number of elements would be less than the amounts reported in this study. The increased number of elements in each model might cause a significantly higher computational cost if it is further used as a geometry model in any physical finite element simulation. As shown in Figure 17 for the cells and Figure 19b for the open pores, the roundness over the microstructures decreases. The pore structure can be analogized to a foam geometry. An example of open-cell foam morphology with a polycrystalline structure was presented in [21].

In summary, a porous geometry is produced based on the initial numerical inputs. If the density is not equal to the anticipated value, further calibration can be performed. The model needs to be verified by the experimental results when employed to accurately predict the relative density.

6. Conclusions

The model approach here provides a simulation tool with the purpose to characterise porous polycrystalline materials. The model can be effectively used as representative volume elements (RVEs) in statistical analysis because of the reproducibility. It is possible to quantitatively analyse different types of porosity because of the ability of the method to simulate open/closed porosity. Due to the adjustability of the model, the accuracy of generated models can be significantly improved and properly validated by experiments. If required, a parametric study may be performed based on the numerical inputs and experimental data.

The novelty of the method stands on its advantage in reproducing a complex structure using the Voronoi tessellation methods and the Coble's model, which are simple and have been widely

accepted. For improvement or modification, any other different Voronoi tessellation algorithm available in the open literature can be replaced by the algorithm used in this article. For instance, the outputs of the software DREAM.3D are potentially compatible with the framework presented here. Either seed points or the Voronoi cells generated by this package can make the model more accurate, as they are based on experimental data such as the location of grains and grain boundaries. It is worth mentioning that to avoid *inevitable* intersections when irregularity increases, the simple algorithm of Loop subdivision surface might be changed with other advanced algorithms.

Acknowledgement

The authors gratefully acknowledge the financial support from the Engineering and Physical Sciences Research Council (Grant No. EP/R041504/1).

References

[1] W. Ehlers, J. Bluhm, Porous media: theory, experiments and numerical applications, Springer Science & Business Media2013.

[2] M. Ardeljan, M. Knezevic, T. Nizolek, I.J. Beyerlein, N.A. Mara, T.M. Pollock, A study of microstructure-driven strain localizations in two-phase polycrystalline HCP/BCC composites using a multi-scale model, International Journal of Plasticity, 74 (2015) 35-57.

[3] X. Peng, Z. Guo, T. Du, W.R. Yu, A simple anisotropic hyperelastic constitutive model for textile fabrics with application to forming simulation, Composites Part B: Engineering, 52 (2013) 275-281.

[4] V.P. Rajan, J.H. Shaw, M.N. Rossol, F.W. Zok, An elastic–plastic constitutive model for ceramic composite laminates, Composites Part A: Applied Science Manufacturing, 66 (2014) 44-57.

[5] D.W. Rosen, Computer-aided design for additive manufacturing of cellular structures, Computer-Aided Design Applications, 4 (2007) 585-594.

[6] P.R. Dawson, Computational crystal plasticity, International journal of solids structures, 37 (2000) 115-130.

[7] R. Logé, M. Bernacki, H. Resk, L. Delannay, H. Digonnet, Y. Chastel, T. Coupez, Linking plastic deformation to recrystallization in metals using digital microstructures, Philosophical Magazine, 88 (2008) 3691-3712.

[8] J.P. Heath, J.H. Harding, D.C. Sinclair, J.S. Dean, Electric field enhancement in ceramic capacitors due to interface amplitude roughness, Journal of the European Ceramic Society, (2018).

[9] Z. Sun, R.E. Logé, M. Bernacki, 3D finite element model of semi-solid permeability in an equiaxed granular structure, Computational Materials Science, 49 (2010) 158-170.

[10] S. Naderi, A. Dabbagh, M.A. Hassan, B.A. Razak, H. Abdullah, N.H.A. Kasim, Modeling of porosity in hydroxyapatite for finite element simulation of nanoindentation test, Ceramics International, 42 (2016) 7543-7550.

[11] R. Al-Raoush, M. Alsaleh, Simulation of random packing of polydisperse particles, Powder technology, 176 (2007) 47-55.

[12] G. Dale, M. Strawhorne, D.C. Sinclair, J.S. Dean, Finite element modeling on the effect of intra-granular porosity on the dielectric properties of BaTiO3 MLCCs, Journal of the American Ceramic Society, 101 (2018) 1211-1220.

[13] V.P. Nguyen, M. Stroeven, L.J. Sluys, Multiscale failure modeling of concrete: micromechanical modeling, discontinuous homogenization and parallel computations, Computer Methods in Applied Mechanics Engineering Geology, 201 (2012) 139-156.

[14] X. Wang, M. Zhang, A.P. Jivkov, Computational technology for analysis of 3D meso-structure effects on damage and failure of concrete, International Journal of Solids Structures, 80 (2016) 310-333.

[15] V. Shulmeister, M. Van der Burg, E. Van der Giessen, R. Marissen, A numerical study of large deformations of low-density elastomeric open-cell foams, Mechanics of Materials, 30 (1998) 125-140.

[16] H. Zhu, J. Hobdell, A. Windle, Effects of cell irregularity on the elastic properties of open-cell foams, Acta materialia, 48 (2000) 4893-4900.

[17] T.F. Willems, C.H. Rycroft, M. Kazi, J.C. Meza, M. Haranczyk, Algorithms and tools for high-throughput geometry-based analysis of crystalline porous materials, Microporous Mesoporous Materials, 149 (2012) 134-141.

[18] T. Wejrzanowski, J. Skibinski, J. Szumbarski, K. Kurzydlowski, Structure of foams modeled by Laguerre–Voronoi tessellations, Computational Materials Science, 67 (2013) 216-221.

[19] M.A. Groeber, M.A. Jackson, DREAM. 3D: a digital representation environment for the analysis of microstructure in 3D, Integrating Materials and Manufacturing Innovation, 3 (2014) 5.

[20] M. Groeber, S. Ghosh, M.D. Uchic, D.M. Dimiduk, A framework for automated analysis and simulation of 3D polycrystalline microstructures. Part 2: Synthetic structure generation, Acta Materialia, 56 (2008) 1274-1287.

[21] J.C. Tucker, A.D. Spear, A Tool to Generate Grain-Resolved Open-Cell Metal Foam Models, Integrating Materials and Manufacturing Innovation, (2019) 1-10.

[22] Q. Du, V. Faber, M. Gunzburger, Centroidal Voronoi tessellations: Applications and algorithms, SIAM review, 41 (1999) 637-676.

[23] E.A. Lazar, J.K. Mason, R.D. MacPherson, D.J. Srolovitz, Complete topology of cells, grains, and bubbles in three-dimensional microstructures, Physical review letters, 109 (2012) 095505.

[24] E. Catmull, J. Clark, Recursively generated B-spline surfaces on arbitrary topological meshes, Computer-aided design, 10 (1978) 350-355.

[25] L. Saucedo-Mora, T.J. Marrow, 3D Cellular Automata Finite Element Method with explicit microstructure: modeling quasi-brittle fracture using Meshfree damage propagation, Procedia Materials Science, 3 (2014) 1143-1148.

[26] T. Trzepieciński, G. Ryzińska, M. Gromada, M. Biglar, 3D microstructure-based modelling of the deformation behaviour of ceramic matrix composites, Journal of the European Ceramic Society, 38 (2018) 2911-2919.

[27] V. Carollo, J. Reinoso, M. Paggi, Modeling complex crack paths in ceramic laminates: A novel variational framework combining the phase field method of fracture and the cohesive zone model, Journal of the European Ceramic Society, 38 (2018) 2994-3003.

[28] S.J.L. Kang, Sintering: densification, grain growth and microstructure, Elsevier2004.

[29] P. Duran, M. Villegas, J. Fernandez, F. Capel, C. Moure, Theoretically dense and nanostructured ceramics by pressureless sintering of nanosized Y-TZP powders, Materials Science Engineering: A, 232 (1997) 168-176.

[30] E. Hammel, O.R. Ighodaro, O. Okoli, Processing and properties of advanced porous ceramics: An application based review, Ceramics International, 40 (2014) 15351-15370.

[31] W.D. Kingery, M. Berg, Study of the initial stages of sintering solids by viscous flow, evaporation-condensation, and self-diffusion, Journal of Applied Physics, 26 (1955) 1205-1212.

[32] F. Thomsen, G. Hofmann, T. Ebel, R. Willumeit-Römer, An elementary simulation model for neck growth and shrinkage during solid phase sintering, Materialia, 3 (2018) 338-346.

[33] J. Bruchon, D. Pino-Muñoz, F. Valdivieso, S. Drapier, Finite element simulation of mass transport during sintering of a granular packing. part I. surface and lattice diffusions, Journal of the American Ceramic Society, 95 (2012) 2398-2405.

[34] H. Zhou, J.J. Derby, Three-Dimensional Finite-Element Analysis of Viscous Sintering, Journal of the American Ceramic Society, 81 (1998) 533-540.

[35] A. Jagota, P. Dawson, Micromechanical modeling of powder compacts: I. Unit problems for sintering and traction induced deformation, Acta Metallurgica, 36 (1988) 2551-2561.

[36] P. Zeng, S. Zajac, P. Clapp, J. Rifkin, Nanoparticle sintering simulations1, Materials Science Engineering: A, 252 (1998) 301-306.

[37] W. Zhang, J. Schneibel, The sintering of two particles by surface and grain boundary diffusion: a two-dimensional numerical study, Acta Metallurgica et Materialia, 43 (1995) 4377-4386.

[38] J. Svoboda, H. Riedel, New solutions describing the formation of interparticle necks in solid-state sintering, Acta Metallurgica et Materialia, 43 (1995) 1-10.

[39] D. Budworth, Theory of pore closure during sintering, Trans. Brit. Ceram. Soc, 6911 (1970) 29-31.

[40] W. Beere, The second stage sintering kinetics of powder compacts, Acta Metallurgica, 23 (1975) 139-145.

[41] Y.U. Wang, Computer modeling and simulation of solid-state sintering: A phase field approach, Acta materialia, 54 (2006) 953-961.

[42] J.L. Johnson, R.M. German, Theoretical modeling of densification during activated solid-state sintering, Metallurgical Materials Transactions A, 27 (1996) 441-450.

[43] R.L. Coble, Sintering crystalline solids. I. Intermediate and final state diffusion models, Journal of applied physics, 32 (1961) 787-792.

[44] T.J. Cashman, NURBS-compatible subdivision surfaces, Cashman, Thomas J., 2010.

[45] C. Loop, Triangle mesh subdivision with bounded curvature and the convex hull property, MSR Tech Report MSR-TR-2001–24, (2001).

[46] K. Döbrich, C. Rau, C. Krill, Quantitative characterization of the three-dimensional microstructure of polycrystalline Al-Sn using X-ray microtomography, Metallurgical and Materials Transactions A, 35 (2004) 1953-1961.

[47] F. Aurenhammer, Voronoi diagrams: a survey of a fundamental geometric data structure, ACM Computing Surveys (CSUR), 23 (1991) 345-405.

[48] M.I. Mendelson, Average grain size in polycrystalline ceramics, Journal of the American Ceramic society, 52 (1969) 443-446.

[49] G. Van Dalen, M. Koster, 2D & 3D particle size analysis of micro-CT images, Unilever Res Dev Netherlands, (2012).

[50] G. Liu, H. Yu, Experimental evaluation of stereological methods for determining 3D grain size and topological distributions, Image Analysis & Stereology, 19 (2011) 91-97.

[51] Z. Chen, X. Wang, F. Giuliani, A. Atkinson, Microstructural characteristics and elastic modulus of porous solids, Acta Materialia, 89 (2015) 268-277.

[52] M.N. Rahaman, Ceramic processing and sintering, CRC press2003.

Figure captions

- Figure 1. The analogy between (a) a typical porous polycrystalline microstructure of sintered magnetic ceramic [27] and a model comprised by Voronoi polygons representing grains (light) and pores (dark).
- Figure 2. (a) Microstructure changes during sintering in three main stages. (b) Tetrakaidecahedron with tubular pores on its edges represents grain structure (Coble's geometrical model) [43].
- Figure 3. Three cubic domains are tessellated to 400 Voronoi cells by different discretization strategies. Also, 2D models are schematically displayed for better visualization of the relationship between Voronoi cells and the generator points.
- Figure 4. Two main steps in Loop subdivision scheme.
- Figure 5. Schematic diagram of the shape transformation of the polygonal Voronoi cell through the fitting B-Spline surface procedure after three iterations. In each iteration, the control points and their connectivity are restructured by the geometry in the previous step.
- Figure 6. VSCs constructed inside the Voronoi cells with no intersection between adjacent cells. For better visualization, the original Voronoi cells are shown in the transparent surface.
- Figure 7. (a) In the unit cell, the shrunk cell vertices (red point) are computed using the original polygon vertices (black points) and the centroid (white point). (b) Two samples of the scaled Voronoi cells (left) and VSCs (right) are shown. The original cells are represented in the transparent surface from.
- Figure 8. The theoretical model (shown in Figure 2b) is simplified and segmented into different parts. The grains and interconnections are represented by polygonal Voronoi cells and prismatic geometries, respectively.
- Figure 9. Two main steps to insert the cohesive prism between the adjacent cells are: (a) detecting the shared vertices and the interface; (b) creating the cohesive interface prism

using the duplicated nodes. L_e is the characteristic length that states the distance between two ends of the prism.

- Figure 10. CIPs (red) are elongated from (a) to (c) while the 50 Voronoi cells (grey) are shrunk by applying different scale factors.
- Figure 11. The presence of end faces of prism fails the merging process and keeps the cells isolated.
- Figure 12. The splined surfaces are generated through the merged Voronoi cells and the pore network is automatically created.
- Figure 13. The schematic depicts the densification curve of a powder compact during three stages of sintering [28].
- Figure 14. Probability density function (PDF) against the normalized grain volume values. The maximum value around the mean value is decreasing while the irregularity is increasing while the number of cells is constant. The models are shown on the side as a guide for the eye.
- Figure 15. Schematic diagram of the geometric relationship between the theoretical and the numerical model parameters.
- Figure 16. 3D cross-sectional view of three models. Where $\mathrm{q} = 0.8$, the model includes open porosity (a); by the variable value of q in a range between 0.8 and 0.99, an open-closed porosity is reconstructed (b); and for $\mathrm{q} = 0.99$, the closed pore system dominates through the structure (c). As an example, the actual digital 3D microstructure of porous LSCF ceramic sintered at 1200 ^{o}C is used for comparison [51]. It was reconstructed using FIB/SEM tomography (d). The planar cross-sectional view of the virtual model is compared to the real microstructure of $\mathrm{CeO_2}$ [52] after incomplete removal of the porosity (e).
- Figure 17. The effect of control points number on the splined surfaces.

- Figure 18. (a) The number against the average equivalent size of the cell is plotted. Similar results are obtained for two levels of irregularity ($d = 0$ and 1). The dotted line is a guide for the eye to show the general trends; (b) The relative density versus the average equivalent cell size is shown for different values of q and d.

- Figure 19. (a) Relative density against the number of control points and the time length to generate model based on a model generated with the configurations of $q = 0.8$, 93 and the mean cell size of 14.7 units. The numbers of elements are also labelled on the data points. The simulations were run on a laptop computer (DELL Latitude 7490) with the specifications of Intel® Core™ i7-8650U 1.90 GHz processor and 16.0 GB RAM; (b) Cross-sections of the open pores before (left) and after (right) 10 steps increasing the number of the control points.

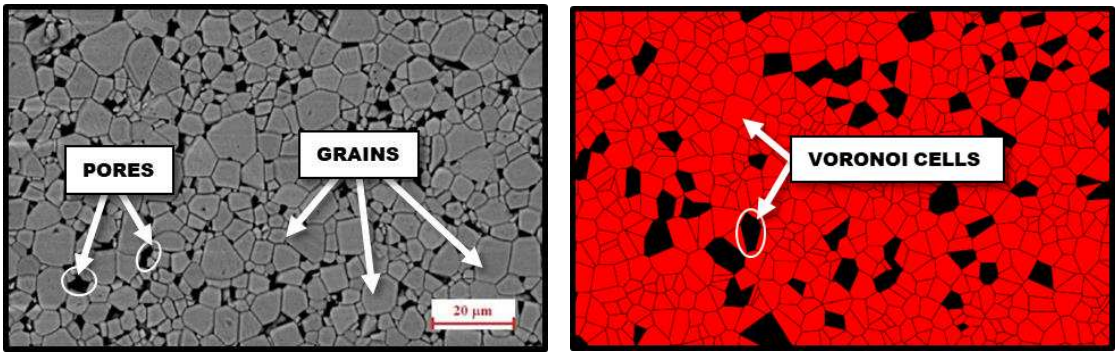

(a) **(b)**

Figure 1. The analogy between (a) a typical porous polycrystalline microstructure of sintered magnetic ceramic [27] and a model comprised by Voronoi polygons representing grains (light) and pores (dark).

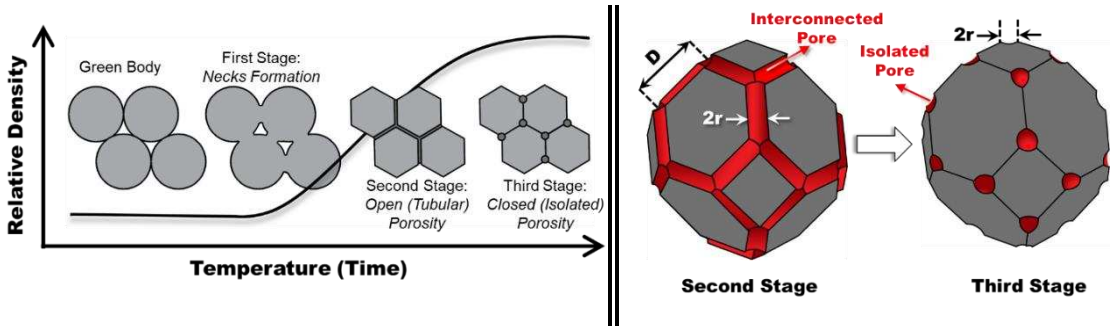

Figure 2. (a) Microstructure changes during sintering in three main stages. (b) Tetrakaidecahedron with tubular pores on its edges represents grain structure (Coble's geometrical model) [43].

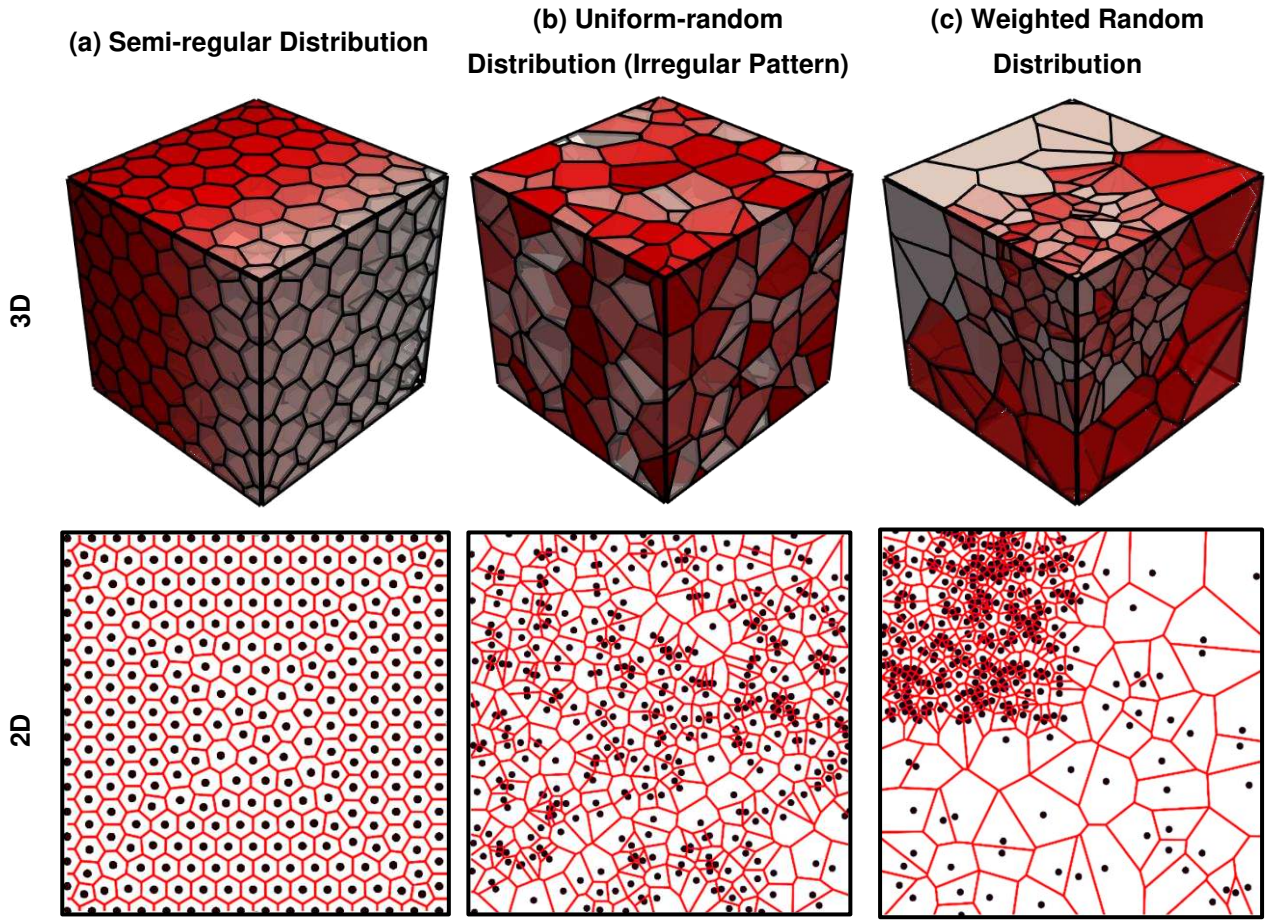

Figure 3. Three cubic domains are tessellated to 400 Voronoi cells by different discretization strategies. Also, 2D models are schematically displayed for better visualization of the relationship between Voronoi cells and the generator points.

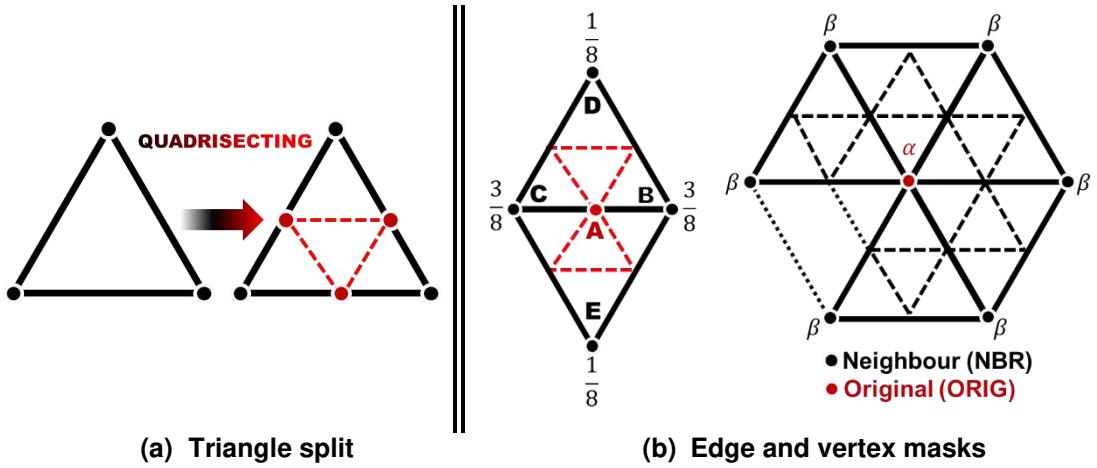

(a) Triangle split **(b) Edge and vertex masks**

Figure 4. Two main steps in Loop subdivision scheme.

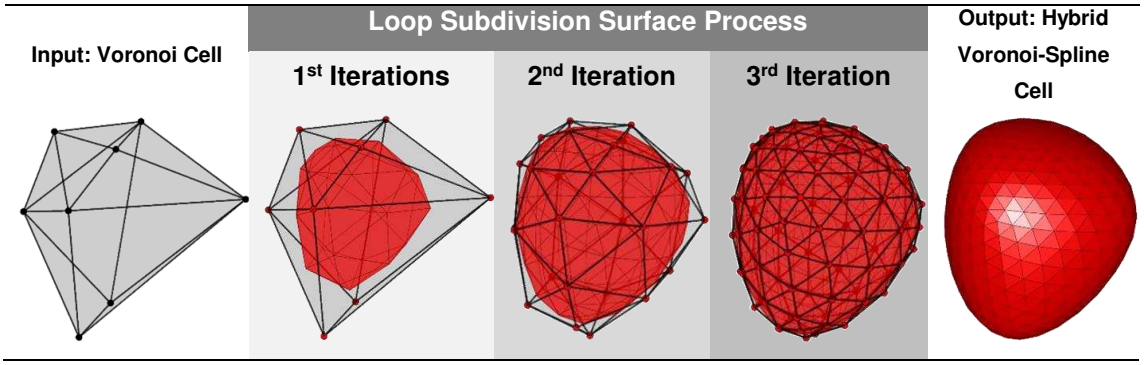

Figure 5. Schematic diagram of the shape transformation of the polygonal Voronoi cell through the fitting B-Spline surface procedure after three iterations. In each iteration, the control points and their connectivity are restructured by the geometry in the previous step.

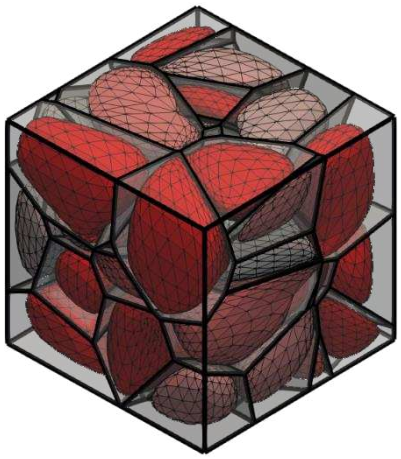

Figure 6. VSCs constructed inside the Voronoi cells with no intersection between adjacent cells. For better visualization, the original Voronoi cells are shown in the transparent surface.

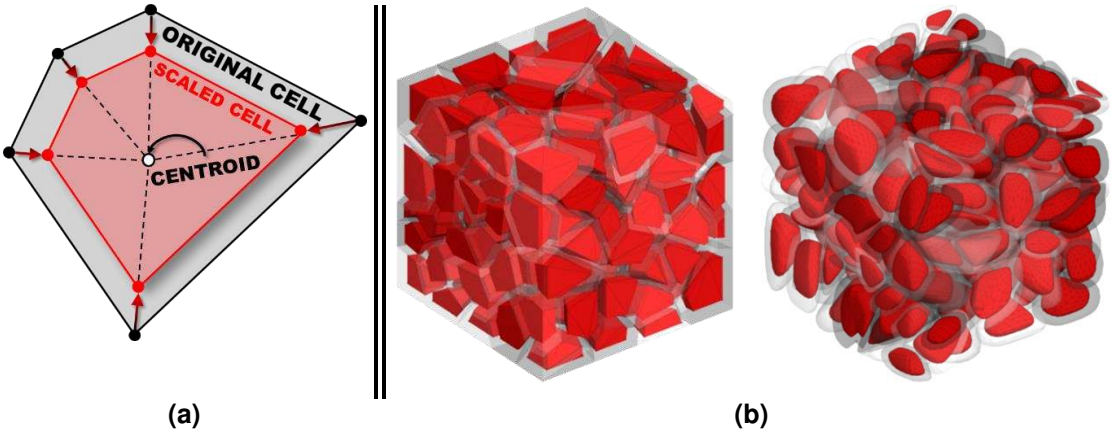

Figure 7. (a) In the unit cell, the shrunk cell vertices (red point) are computed using the original polygon vertices (black points) and the centroid (white point). (b) Two samples of the scaled Voronoi cells (left) and VSCs (right) are shown. The original cells are represented in the transparent surface from.

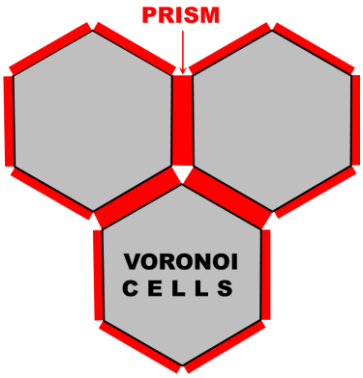

Figure 8. The theoretical model (shown in Figure 2b) is simplified and segmented into different parts. The grains and interconnections are represented by polygonal Voronoi cells and prismatic geometries, respectively.

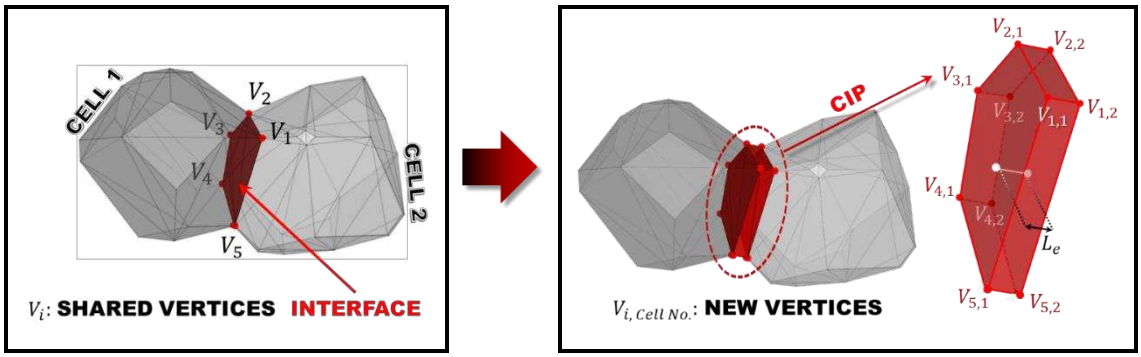

(a) **(b)**

Figure 9. Two main steps to insert the cohesive prism between the adjacent cells are: (a) detecting the shared vertices and the interface; (b) creating the cohesive interface prism using the duplicated nodes. L_e is the characteristic length that states the distance between two ends of the prism.

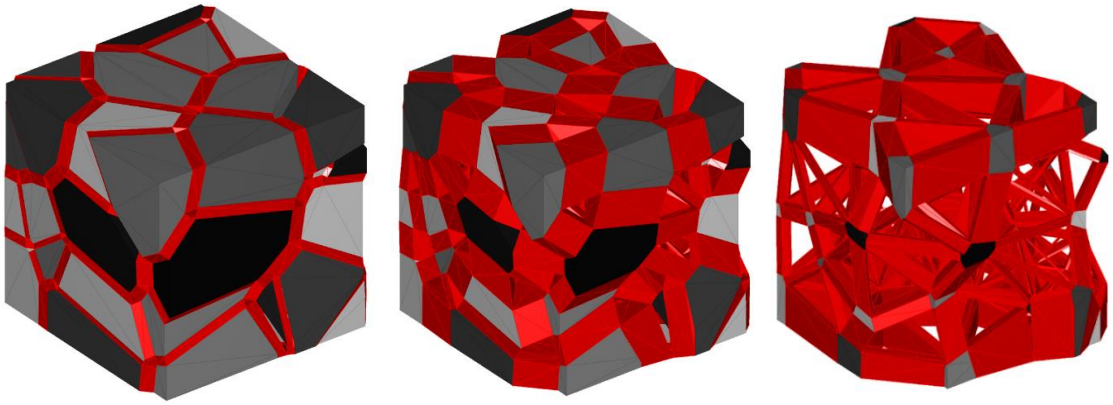

(a) $q = 0.8$ **(b)** $q = 0.5$ **(c)** $q = 0.2$

Figure 10. CIPs (red) are elongated from (a) to (c) while the 50 Voronoi cells (grey) are shrunk by applying different scale factors.

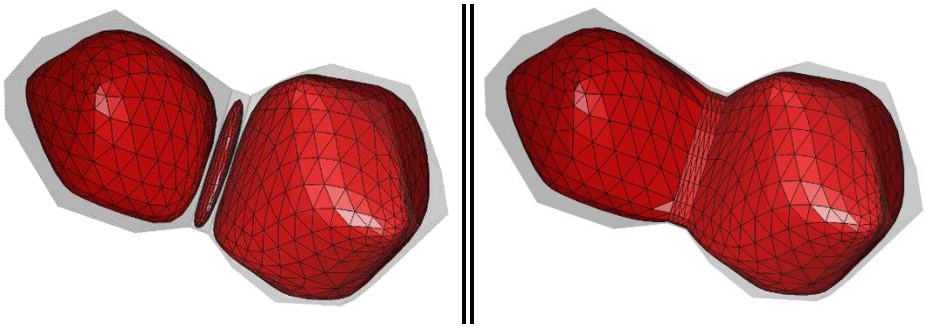

(a) With End Faces **(b) Without End Faces**

Figure 11. The presence of end faces of prism fails the merging process and keeps the cells isolated.

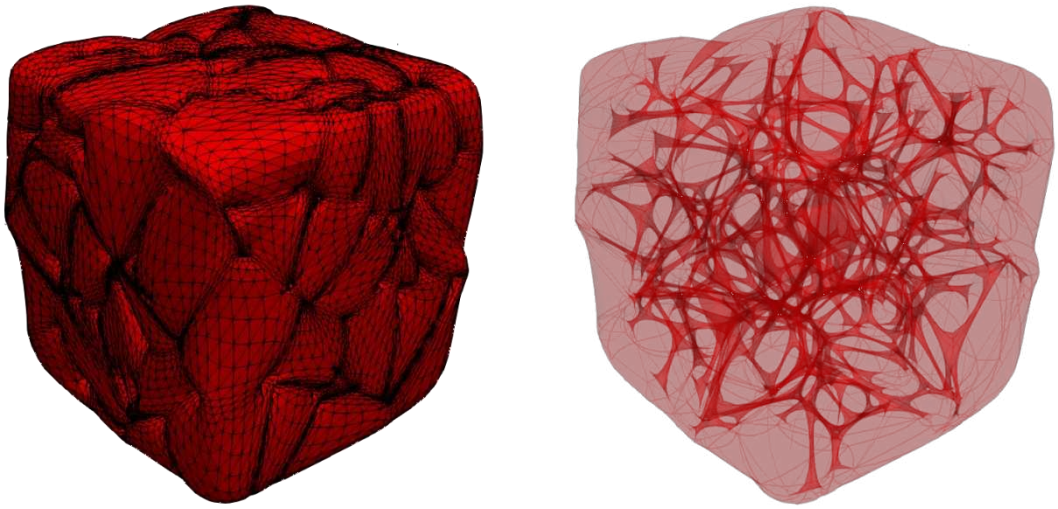

(a) 3D Mesh Surface **(b) Transparent Form**

Figure 12. The splined surfaces are generated through the merged Voronoi cells and the pore network is automatically created.

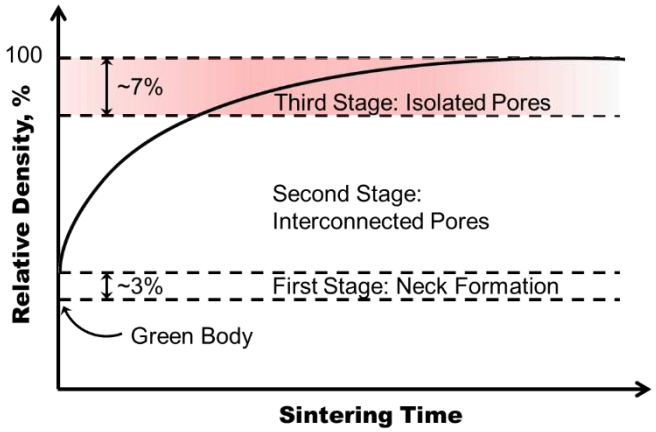

Figure 13. The schematic depicts the densification curve of a powder compact during three stages of sintering [28].

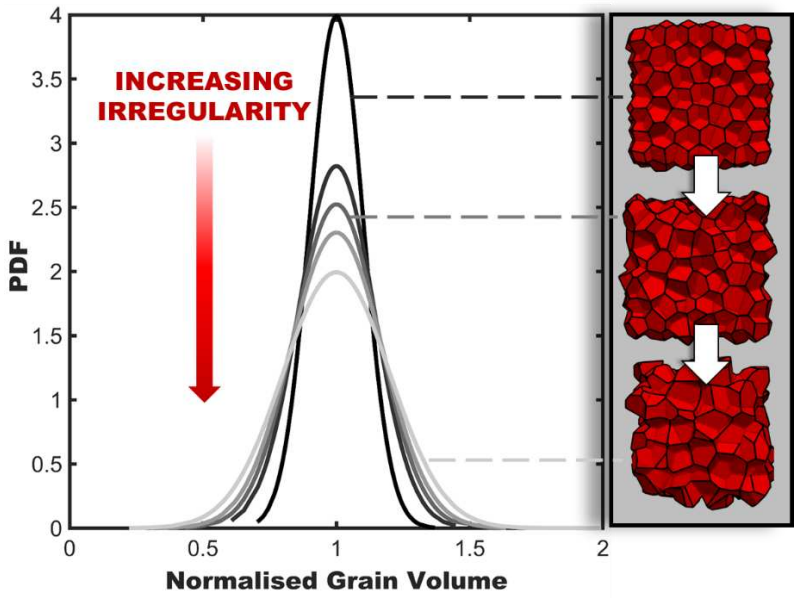

Figure 14. Probability density function (PDF) against the normalized grain volume values. The maximum value around the mean value is decreasing while the irregularity is increasing while the number of cells is constant. The models are shown on the side as a guide for the eye.

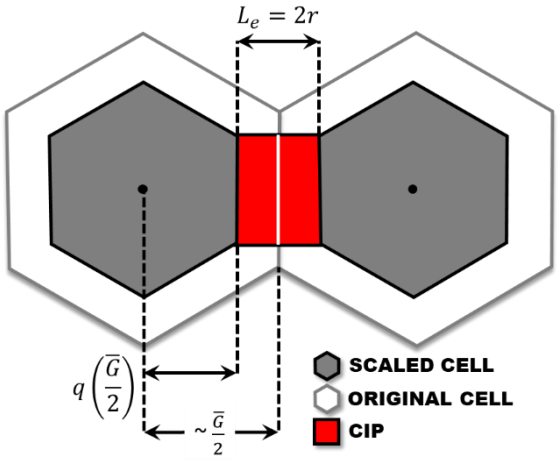

Figure 15. Schematic diagram of the geometric relationship between the theoretical and the numerical model parameters.

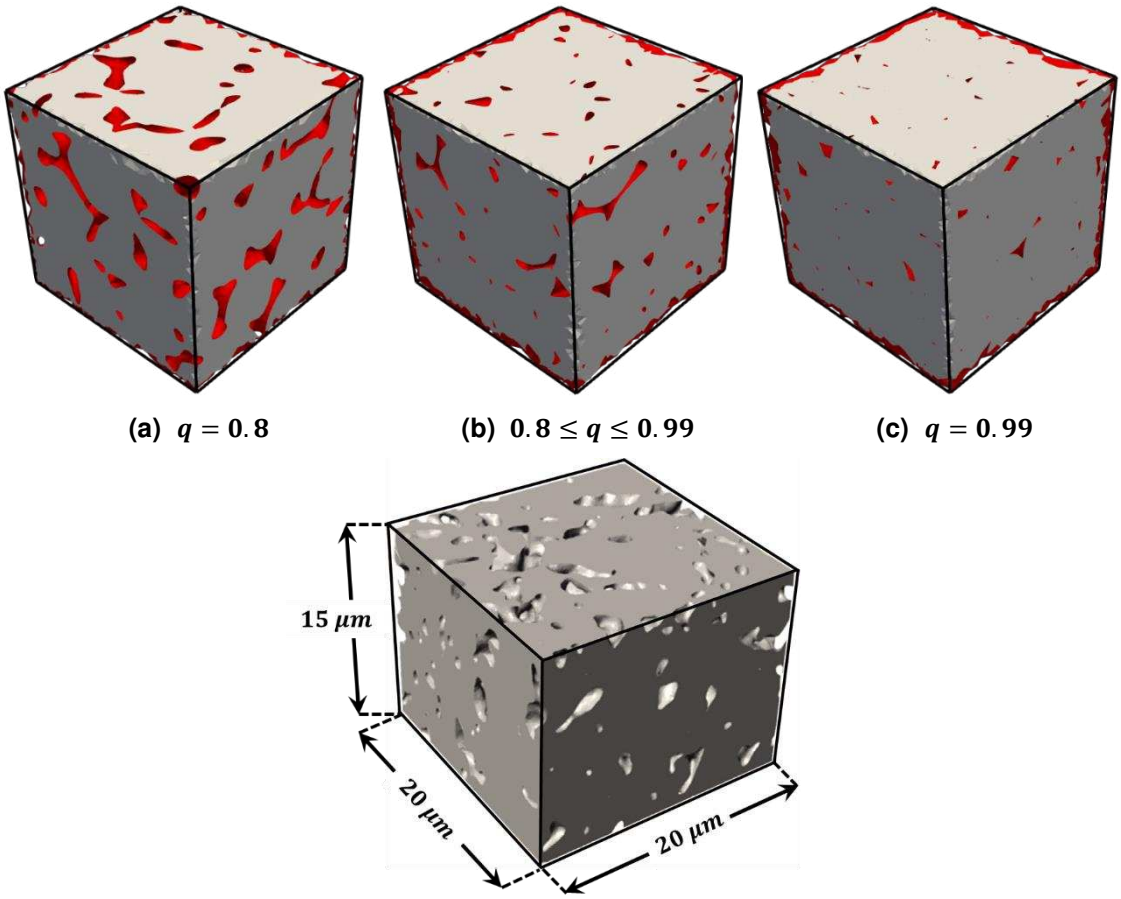

(a) $q = 0.8$ **(b)** $0.8 \leq q \leq 0.99$ **(c)** $q = 0.99$

(d) $Relative\ density = 84.8 \pm 1.2\%$, $ESD = 1700 \pm 630\ nm$

(e)

Figure 16. 3D cross-sectional view of three models. Where $q = 0.8$, the model includes open porosity (a); by the variable value of q in a range between 0.8 and 0.99, an open-closed porosity is reconstructed (b); and for $q = 0.99$, the closed pore system dominates through the structure (c). As an example, the actual digital 3D microstructure of porous LSCF ceramic

sintered at 1200 °C is used for comparison [51]. It was reconstructed using FIB/SEM tomography (d). The planar cross-sectional view of the virtual model is compared to the real microstructure of CeO_2 [52] after incomplete removal of the porosity (e).

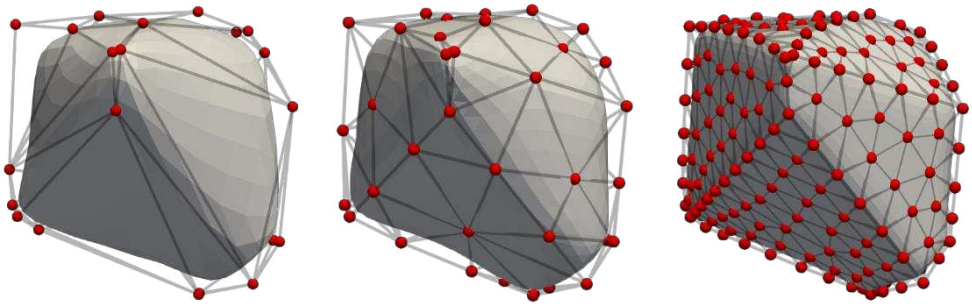

(a) 26 Points **(b) 48 Points** **(c) 228 Points**

Figure 17. The effect of control points number on the splined surfaces.

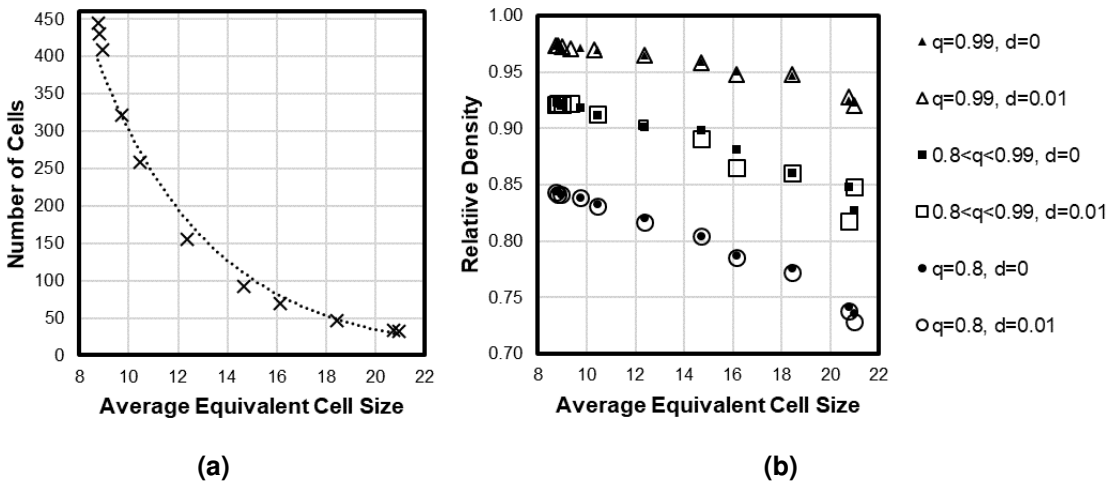

Figure 18. (a) The number against the average equivalent size of the cell is plotted. Similar results are obtained for two levels of irregularity ($d = 0$ and 1). The dotted line is a guide for the eye to show the general trends; (b) The relative density versus the average equivalent cell size is shown for different values of q and d.

(a)

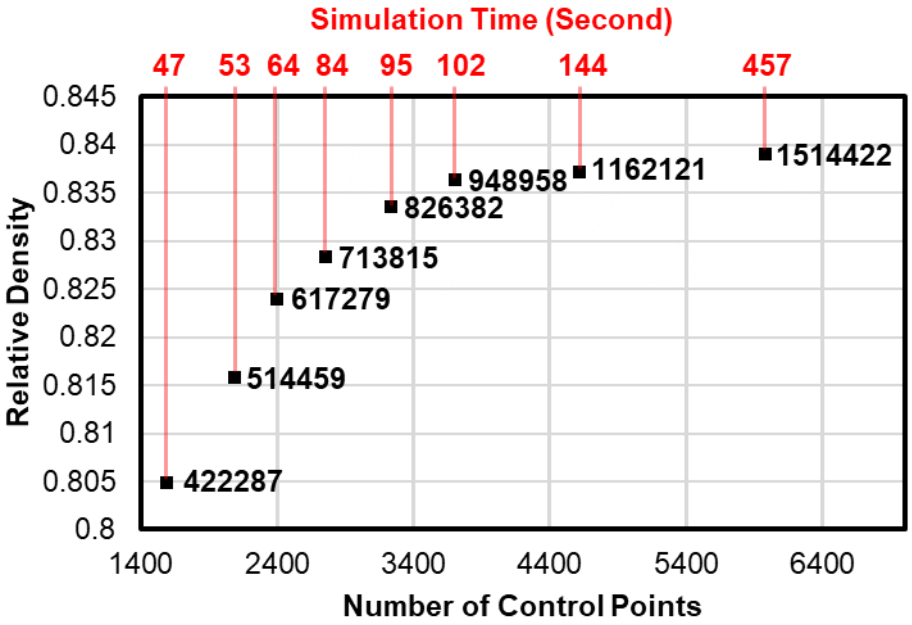

(b)

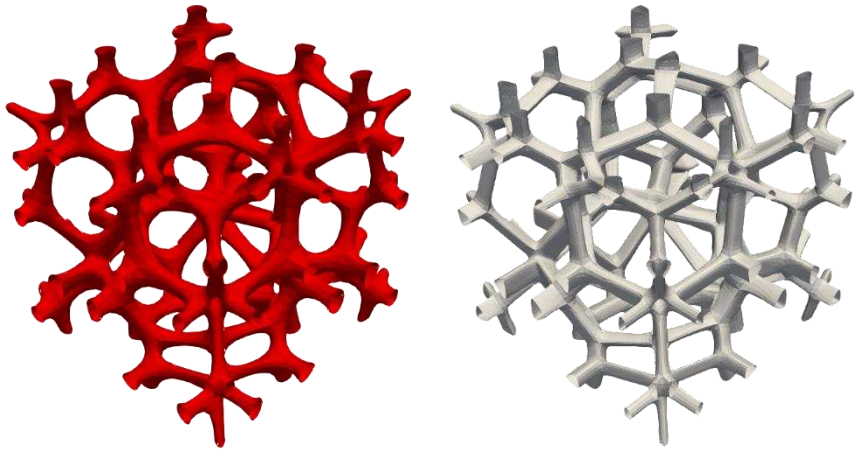

1594 Points 5978 Points

Figure 19. (a) Relative density against the number of control points and the time length to generate model based on a model generated with the configurations of $q = 0.8$, 93 and the mean cell size of 14.7 units. The numbers of elements are also labelled on the data points. The simulations were run on a laptop computer (DELL Latitude 7490) with the specifications of Intel® Core™ i7-8650U 1.90 GHz processor and 16.0 GB RAM; (b) Cross-sections of the open pores before (left) and after (right) 10 steps increasing the number of the control points.